



Supplementary Materials for

Eddy-driven subduction exports particulate organic carbon from the spring bloom

Melissa M. Omand, Eric A. D'Asaro, Craig M. Lee,
Mary Jane Perry, Nathan Briggs, Ivona Cetinić, Amala Mahadevan*

*Corresponding author. E-mail: amala@whoi.edu

Published 26 March 2015 on *Science Express*
DOI: 10.1126/science.1260062

This PDF file includes:

Materials and Methods
Figs. S1 to S18
Table S1
References

MATERIALS AND METHODS

Here we describe, in Section S1, observations from the North Atlantic Bloom study (NAB08) used to detect intrusions of particulate organic carbon (POC) rich water in the pycnocline. We provide details of the data analysis. In Section S2, we describe the modeling, which shows how surface POC-rich water is subducted by the dynamic eddying flow field. Finally, in Section S3, we describe the estimation of POC export caused by eddy-driven subduction, and compare it with estimates of sinking POC flux.

S1 Observations and Analysis

S1.1 Field Experiment

The North Atlantic Bloom study of 2008 (NAB08) was an intensive observational program characterizing the spring phytoplankton bloom south of Iceland. An array of Seagliders – self-propelled, buoyancy-driven autonomous under-water vehicles (39) – surveyed a patch-following reference frame defined by an autonomous, subsurface Lagrangian float. These instruments were deployed from R/V *Bjarni Saemundsson* on 4 April 2008 (yearday 95; yearday 1 = 1 January 2008), and were supported by ship-based measurements of physics, biology, and chemistry from R/V Knorr in May.

The experiment was designed to sample the onset and evolution of the North Atlantic Spring phytoplankton bloom. A schematic of the winter to spring transition is shown in Fig. S1. Phytoplankton concentration within the mixed layer, as assessed by chlorophyll fluorescence, Chl F, was low in mid-winter, and increased rapidly around yearday 110, marking the onset of the spring bloom. Between yearday 114 and 134, the mixed layer (spatially averaged across the four gliders and defined at the depth with $\Delta\sigma_t = 0.05$ relative to 10 m) shoaled from 150 to 50 m. Net community production increased by a factor of two, and was largely confined to above the mean euphotic depth of 45 m (23). Diatoms dominated the early bloom, which terminated around yearday 135 (23, 31) due to exhaustion of silicate and generated a sinking flux of large aggregates reaching $514 \text{ mgC m}^{-2} \text{ d}^{-1}$ at 100 m depth (21). This event marked the start of an overall decline in depth-averaged phytoplankton carbon, while the continued stratification induced by surface warming led to an increase in the carbon concentration near the surface. The large aggregates generated spikes in the backscatter and Chl F, with a coherent signal seen to descend at $\sim 75 \text{ m d}^{-1}$ (21). Loss of the diatoms gave way to a recycling-based community of phytoplankton dominated by small cells (40), which did not exhibit measurable sinking.

S1.2 Glider data

The gliders dove to 1000 m at descent rates of 0.1 m s^{-1} and travelled horizontally at an average speed of 0.32 m s^{-1} , surfacing every 4 to 6 h. They were subject to advection by currents, resulting in dive translations of 1 to 15 km. The difference between the predicted (based on

dead reckoning) and actual locations at which the gliders surface, provides an estimate of the depth-averaged currents (DAC). Overall, the DACs were well correlated with the ship-board ADCP (*Gray et al. in preparation*). Between yearday 128 and 142, the four gliders remained within an 80 km \times 80 km region, densely mapping the hydrography around the mixed layer float as it was entrained within an anticyclone. DACs from this two week period were used to create an objective map of the dynamic height, with a decorrelation scale of 18 km and a signal to noise ratio of 0.3 (41). Mapped points with low skill (< 0.70) were excluded.

The gliders carried sensors that measured temperature, salinity, backscatter, Chl-F, dissolved oxygen and photosynthetically available radiation (PAR). Backscatter is used as a proxy for particulate organic carbon (POC); its derivation is described in *Briggs et al., 2011 (21)*. Throughout the cruise, POC and chlorophyll-a were sampled and analyzed following JGOFS protocols. The Biological and Chemical Oceanography Data Management Office data system (BCO-DMO) contains detailed calibration reports and data (<http://data.bco-dmo.org/jg/dir/BCO/NAB08/>). Here, we use the backscatter signal that is filtered of large spikes associated with aggregates of particulate organic matter (21). The filtered backscatter signal is attributed to the small size class of particulate organic matter, which, due to its associated Chl-F, is interpreted as phytoplankton-derived POC (sometimes referred to as phytoplankton carbon).

On each glider, WET Labs BB2F ECO pucks measured chlorophyll-a fluorescence with excitation at 470 nm and the volume scattering function at a centroid angle of 12.41 at wavelengths of 470 and 700 nm. Dissolved oxygen (DO) was measured with Aanderaa 3830 optodes calibrated against the float and ship. The Apparent Oxygen Utilization was calculated according to $AOU = DO_{sat} - DO_{meas}$. In addition to factory calibration of all sensors before and after the deployment, 11 independent inter-calibrations between the Seaglider and ship optical sensors were performed.

S1.3 Identifying subsurface features from glider profiles

Some of the glider profiles showed subsurface features of POC and dissolved oxygen. We considered a subsurface feature to be present if the glider profile satisfied the following criteria: It had a subsurface local maximum in POC that was located below the euphotic zone (as defined by the 1% PAR light level measured on the mixed layer float) and the bottom of the mixed layer depth (as defined by $\Delta\sigma = 0.05$ from 10 m). The vertical extent of each feature was defined as $\pm 0.005 \text{ kg m}^{-3}$ on either side of the POC maxima, a criterion that successfully encompassed most of the features. These features were very often associated with temperature-salinity anomalies, elevated Chl F, and elevated dissolved oxygen (DO). Covariation of physical (42) and biological tracers (43) is a ubiquitous feature of the near-surface ocean, resulting from the stirring of properties along isopycnals by eddies and filaments (27). The co-location of spice and oxygen anomalies (which do not sink) with the POC suggests that the features were formed by intrusions extending downward and laterally from the surface. A potential temperature (θ) versus salinity diagram of the profiles has a distinctive s-shape at the local apparent oxygen utilization (AOU) minimum (colors) delineating the surrounding water mass from the

intrusion (Fig. S2a). Flament (2002) (44) defined a state variable called ‘spiciness’ to describe co-variation of temperature and salinity that is least correlated with the density field, and is a useful indicator of interleaving of water masses. Over the vertical scale of the features we analyzed, we found that POC and AOU are more correlated with spice than with potential density (σ_t , Fig. S2b). A budget of spice can be applied to reveal the underlying diapycnal or isopycnal mixing that also alters the variability of biological tracers on isopycnals (45). Thirty three of the subsurface features were on the same water mass defined by $\sigma_t = 27.48 \pm 0.005 \text{ kg m}^{-3}$, with co-located spice, POC and DO anomalies. The mean depth of each of these features varies from -80 m to -300 m (Fig. S3). The upper extent of the shallowest features outcrop into the mixed layer (see yearday 130, Fig. 1c), and occur near the north-west edge of the anticyclone. These shallow features also contained the maximum POC and DO observed on this water mass (not shown) and may represent the source location for those features observed later.

S1.4 Evaluating remineralization

An analysis of the changes in biological properties on the subducted water mass (in the Lagrangian frame) allows us to evaluate a remineralization timescale. The apparent oxygen utilization (AOU) is a measure of the amount of production/respiration that has occurred on a water parcel since ventilation at the surface. Once isolated at depth from the atmosphere, changes in the AOU are driven primarily by biological processes and not by mixing, heating or cooling of the water. We find a trend of increasing AOU on subducted water masses, even as the surface water AOU is decreasing (Fig. 2). This suggests that the subducted water remains isolated from the surface over the duration of the observations. All of the features were below the euphotic zone where photosynthesis is not significant, and the change in AOU is likely due to respiration of the POC. We estimate respiration rates of $0.4 \text{ mmol O}_2 \text{ m}^{-3} \text{ d}^{-1}$. Quantification of the remineralization rate provides a benchmark against which we can evaluate the fate of the carbon exported by eddies. The net export of POC through eddy-driven subduction depends both on the vertical transport of organic material into the interior, and also on retention over remineralization timescales or longer. Over seasonal scales, the transfer of fluid from the mixed layer into the stratified interior is most often described in terms of large-scale water mass transformation and advection (10–12). On the opposite end of the spectrum, dynamics which vertically displace water, but occur on timescales more rapid than remineralization (e.g. semi-diurnal and higher frequency internal waves) will not lead to a net export. We find that eddy-driven subduction falls between these two timescales, and that locally subducted water remains below the euphotic layer for sufficiently long to experience remineralization of the POC.

S1.5 Isopycnal depth and tilt

Since a group of gliders were profiling in the vicinity of the float, we can estimate the tilt of an isopycnal surface, $\sigma=27.48$, by determining the depths at which 3 concurrently profiling gliders intersect the isopycnal surface (Fig. S4a) and fitting a surface through the 3 points. For each Seaglider profile, we find the profiles from the other gliders that occurred nearest in time

(within 3 hours) and fit a plane between the coordinates of the $27.48 \pm 0.005 \text{ kg m}^{-3}$ isopycnal ($x_{sig}, y_{sig}, z_{sig}$) yielding the isopycnal tilt (Γ , Fig. S4c) and orientation (not shown).

S1.6 Spatial Aliasing

Our isopycnal tilt estimates depend, in part, on the separation distances between the gliders. This can be problematic, because at large gliders separations, the tilts are likely to be underestimated due to spatial aliasing. As has been shown in other studies (29), the lateral buoyancy gradients (hence the isopycnal slopes) are scale-dependent. As the length-scale (Δx) over which they are evaluated is decreased, the gradients (or tilts) increase (Fig. S5a). The isopycnal tilt was computed using the NAB08 gliders (black points) and from the model at 1 to 60 km spacing along a latitudinal slice (gray points). We find that the isopycnal tilts may be underestimated by as much as a factor of five when the mean glider separation is greater than 40 km. This separation was exceeded for 7% of the tilts calculated between yeardays 110 and 150 (Fig. S5b), and these were excluded from the analysis.

A time series of the isopycnal depth, glider separation Δx and isopycnal tilt is shown in Fig. S4. Overall, the glider separations were largest before yearday 126, which may contribute to the lower Γ during this period (Fig. S4c). We cannot correct for this bias in our analysis, and thus the glider-based estimates of Γ and flux are compared with the model only in a statistical sense (Fig. S6). A more regular glider spacing, or a larger fleet of gliders may improve this issue in future studies.

S1.7 Filtering Internal Waves

Vertical isopycnal oscillations driven by internal waves are ubiquitous throughout the world oceans. Most of this energy is contained within the near-inertial and tidal bands. A half-wavelength of the internal tide ($\lambda \sim 75$ to 150 km) is comparable to the glider separation distance which varied from 2 to 75 km between yeardays 120 and 150 (Fig. S5b). The isopycnal tilts we calculated could be altered by internal wave displacements. These internal wave-driven motions of the isopycnal surfaces are periodic and would have little impact on a net flux of POC. Here we attempt to evaluate how strongly internal waves affect our estimate of the isopycnal tilts. The semi-diurnal internal tide propagates at a speed that is roughly ten times larger than the translation speed of the gliders, which make translations of 1 and 15 km over a dive lasting about 5 hours, thereby traveling horizontally at an average speed of 0.32 m s^{-1} . Thus, we regard the gliders as stationary profilers relative to the internal tide. At the NAB08 latitude, less than 5% of the total variance is observed at timescales less than the inertial period (13.5 hours, Fig. S7). We use a modified PL64 low-pass filter with a half-max width of 18 hrs (46) to retain only the sub-inertial variability on the isopycnal depth from each glider (Fig. S8a). We find that the amplitude and variability in Γ are not significantly affected by the low pass filter (Fig. S8c), suggesting that the presence of internal waves did not generate a bias. Care should be taken to consider internal waves when interpreting isopycnal displacements elsewhere.

S1.8 Sinking flux and total POC export estimated during NAB08 and NABE (1989)

Sinking and total export of carbon was measured at NAB08 and during previous experiments using a variety of optical, radio-isotope, modeling, and sediment trap based methods. The results of some of these efforts are summarized in Table S1. As demonstrated in this Table, the broad range of methodologies for estimating export flux makes direct comparisons challenging. Overall, NAB08, captured export sinking events that resulted in larger estimates than the temporally- and spatially-averaged climatologies from satellite (Fig. S18b). The Lagrangian float in the NAB08 experiment intercepted and followed an elevated patch of Chl over weeks. During this period, sinking export at 100 m of large particulates from a short-lived diatom bloom (described in S1) resulted in a flux of $514 \text{ mgC m}^{-2} \text{ d}^{-1}$ at 100 m (21). Concurrent estimates from NAB08 nitrate, POC and dissolved oxygen budgets suggest that the total carbon export peaked at $984 \text{ mgC m}^{-2} \text{ d}^{-1}$ (23), and export diagnosed from ^{234}Th disequilibria over a similar period (in May) was up to $500 \text{ mgC m}^{-2} \text{ d}^{-1}$ (31). Similarly, during the JGOFS NABE campaign, export flux peaked at $492 \text{ mgC m}^{-2} \text{ d}^{-1}$ in early May (32).

S2 Modeling

This study uses a three-dimensional, nonhydrostatic, Process Study Ocean Model (PSOM) (13). The model domain is $480 \text{ km} \times 96 \text{ km}$ in extent and 1000 m deep. The model uses a stretched grid with 32 levels ranging in thickness from 2.5 m near the surface to 50 m at the lowermost level, and the horizontal grid resolution is 1 km. Boundary conditions are periodic in the East-West direction with walls at the Northern and Southern boundaries. The model is integrated numerically with a time step of 432 s and evolves the density, free-surface height, pressure, and three-dimensional velocity fields from an initial state, subject to the momentum and buoyancy fluxes applied through the boundary conditions at the surface. The biological model (26) expressed in terms of carbon concentration, contains light-dependent growth ($\mu_{max} = 0.536 \text{ d}^{-1}$) and a constant mortality ($m = 0.0748 \text{ d}^{-1}$). This model is similar to what was used in (7); a previous study of stratification and bloom initiation, where the model physics was evaluated against observations. Here, we analyze the period after the onset of the bloom to study the fate of the non-sinking phytoplankton carbon.

To start with, there is almost no POC in the mixed layer (there is only a negligibly small seed population of phytoplankton). Phytoplankton grows with a light-dependent growth rate. There is no nutrient-limitation in this model, since our observations showed sufficient nutrients were present at the time of restratification. Light decays exponentially, with an attenuation coefficient of 0.059 per m and 0.041 per (mg Chl /m^2) . Our model assumes that water within the mixed layer (ML) is well mixed and therefore receives the same amount of light (which is the average light over the ML). The mixed layer depth is diagnosed using a criteria that the density difference be 0.01 kg/m^3 from the surface. As the mixed layer is restratifying, the light distribution, and growth rate is highly variable in depth. It is much larger in regions with shallow mixed layers, and is low beneath the ML. The POC that results has a strong vertical

gradient over the upper 200 m. Regions with deep ML, show very little enhancement in the POC, whereas shallow ML have enhanced POC. Further details about the model are in (7).

S2.1 Model-Data Comparison

The time series of POC and σ_t averaged between the four gliders within the upper 50 m (black line, Fig. S9) follows the spatially averaged modeled variables (solid gray line, Fig. S9) largely within one standard deviation (dashed gray lines). To compare the variability sampled by the gliders, we simulated the NAB08 Seaglider trajectories with virtual gliders in the model domain. We computed the virtual glider DACs by vertically averaging the model currents over each dive, weighted by the time the Seaglider spends at various depths. The model-simulated DACs (gray bars, Fig. S6a) have a similar range of amplitude to the observed DACs, with a normal distribution centered at $14 \pm 5 \text{ cm s}^{-1}$. The observed DACs were more bimodal, reflecting a low-frequency shift in currents due to the mesoscale flow field that is not captured in the model. We examined the depth of the $27.48 \pm 0.005 \text{ kg m}^{-3}$ isopycnal throughout both the Seaglider and virtual glider trajectories (Fig. S6b). Though both had a mean depth of roughly 350 m, the NAB08 gliders observed this density of water significantly deeper (at depths exceeding 450 m) during the early stage of the observations and then traveled to the North, where this isopycnal was shallower (see Fig. S4a). Again, this large-scale slope in the isopycnal surfaces is not in our process model. The observed (glider) POC on this isopycnal had a very similar distribution to the model sampled by virtual gliders, occasionally containing concentrations that exceeded $50 \text{ mgC m}^{-2} \text{ d}^{-1}$ (Fig. S6c).

S2.2 Particle-tracking in the model to quantify re-entrainment by eddies

The implications of eddy-driven POC hinge upon knowing how long the POC remains subducted before becoming re-entrained back into the mixed layer. In the model, a net downward eddy-flux of POC occurs because most regions of high POC anomaly are correlated with downward velocities and vice versa (Fig. S10c, blue areas). In fewer regions, the flux is in the opposite direction (Fig. S10c, red areas). This upward flux of POC, can be thought of as re-entrainment of high POC that was previously subducted. However, the POC tracer in the model does not quantify the time that the water remained subducted. Instead, we used water-following particles within PSOM (courtesy Jinbo Wang). 10,000 particles were seeded randomly throughout the 93 m depth level on day 120. The mixed layer depth at the location is determined at the nearest x-y grid cell to each particle. Particles that are initially below the mixed layer (ML) are excluded, leaving $n=6934$ particles. As restratification progressed, the number of particles below the ML steadily increases (Fig. S11a). After 12 days, 72% of the particles are below the ML. 22% of the particles that left the ML, are re-entrained at some later date, and most of these return within 2 days (Fig. S11b). However, because they were near the base of the ML after re-entrainment, these particles are also more likely to rapidly be subducted again.

S3 Export of POC by eddy-driven subduction

The observation that subducted features of POC lie along isopycnal surfaces (Fig. 1d) is consistent with what occurs in our model. Eddy-driven subduction of POC occurs by advection of POC along sloping isopycnal surfaces. There is a strong vertical gradient in POC, which is produced near surface. The surface waters that are transported downward are rich in POC, whereas waters transported upward toward the surface are generally devoid of POC. This results in a net downward flux of POC. The downward flux of POC can be estimated by multiplying the downward component of the velocity by the POC anomaly. Since the flow field beneath the base of the mixed layer is largely along-isopycnal, its downward component can be estimated by multiplying the along-isopycnal velocity by the slope of the isopycnal surface. This analysis was performed for the period right after the onset of stratification (yearday 110), when isopycnal surfaces in the mixed layer were no longer vertical, and had begun to slump (7).

S3.1 Eddy-driven POC flux from observations

The downward component of the along isopycnal flux of POC is estimated as $\text{Flux} \sim [POC] \Gamma U_s$. We take the average magnitude of the depth averaged currents (DAC) between the gliders to be representative of U_s for this estimate, and similarly use the average POC amongst the three gliders for $[POC]$. The distribution of flux estimates from the observations (white), the virtual gliders (gray) and the model (yellow) is shown in Fig. S12.

S3.2 Eddy-driven POC flux from the model

The vertical POC flux in the model is estimated at each depth bin from the covariance of the vertical velocity anomaly w' (Fig. S10a) and the POC anomalies ($c' = POC - \overline{POC}$, where the overbar indicates a horizontal average over the domain (Fig. S10b)). The product of these represents the instantaneous vertical flux. At 70 m depth over a 100 km \times 100 km subdomain, $w'c'$ varies with the eddy field (Fig. S10c). The majority of regions indicate a negative correlation (blue colors, Fig. S10c), which corresponds to regions where positive POC anomalies are advected down or negative POC anomalies are advected up. Thus, the spatially-averaged net flux $\langle w'c' \rangle$ is negative (downwards). Histograms of POC flux using the glider-based and model-based methods (Fig. S12) indicate a skewed distribution of flux events, with large fluxes occurring infrequently. The mean eddy-driven export from both the model and data predicts 90.1 and 82.2 $\text{mgC m}^{-2} \text{d}^{-1}$ respectively.

S3.3 Generalized scaling for the eddy-driven POC flux

Deep wintertime mixed layers are homogenized vertically by turbulent mixing. But, they harbor horizontal density (buoyancy) gradients. For example, in the subpolar oceans, heavier (colder) water toward the poles gives rise to an (approximately meridional) lateral density gradient, which takes the form of numerous fronts (where the lateral density gradient is more intensified

as compared to the background). Recent work has shown that lateral density gradients within the surface ML become unstable (47, 48) and generate ML eddies that tap the available potential energy (APE) in the fronts. The instabilities are initially 1 to 10 km in horizontal extent, as deep as the ML, and grow on a time scale of days. These eddies cause a net slumping of the wintertime (nearly vertical) isopycnal surfaces, and slide lighter water above heavier water, stratifying the ML (29) on a time scale of weeks.

The intensification of fronts on the peripheries of ML eddies drives secondary ageostrophic circulations, generating vertical velocities of $O(30 \text{ m d}^{-1})$ and ageostrophic cross-front flows of 3 to 5 cm s^{-1} (15). This ageostrophic flow is largely along isopycnal surfaces and carries water from the surface layer, below and across the front, and delivers its contents to the stratifying interior (19). Similarly, the secondary circulations transport water from the base of the mixed layer to the surface. Since POC is produced in the sunlit surface layers, there is a strong vertical gradient in POC. This results in a net downward flux of POC.

The downward eddy-driven POC $Flux = \langle w'POC' \rangle$ can be parameterized in terms of the buoyancy flux $\langle w'b' \rangle$ due to ML eddies. Here, buoyancy $b \equiv -g\rho'/\rho_0$, where ρ_0 is a reference density and ρ' is the density anomaly. The magnitude of the lateral (cross-front) buoyancy gradient $|\nabla_H b| = M^2$, and the vertical buoyancy gradient $b_z = N^2$, which is the buoyancy frequency squared. The vertical flux of buoyancy $\langle w'b' \rangle$ (averaged along a front as denoted by angled brackets) due to ML eddies is largely along (sloping) isopycnals and is given by (28, 29)

$$\langle w'b' \rangle \sim \psi_e |\nabla_H b| = \psi_e M^2, \quad (1)$$

where the overturning (eddy-driven) streamfunction ψ_e due to mixed layer eddies has been parameterized by Fox-Kemper et al. (29) as

$$\psi_e = C_e \frac{M^2 H^2}{f}. \quad (2)$$

Here H is the mixed layer depth, f is the Coriolis parameter, and $M^2 = \nabla_H b$ is the lateral (cross-front) buoyancy gradient. C_e is an empirically-derived scaling coefficient that was found (29) to lie in the range 0.06–0.08. Here, we choose $C_e = 0.08$. The parameterization for the ML-eddy-driven stratification has been tested and successfully implemented (49) in a number of global climate models. To account for the varying grid size of these coarser resolution models and to correct for the weaker lateral buoyancy gradients from under-resolved fronts, Fox-Kemper et al. (49) introduce an additional scaling factor $\Delta x/L_s$, where Δx is the grid resolution and L_s is the submesoscale frontal width. Thus, for coarser resolution fields where $\Delta x > L_s$, (49),

$$\psi_e^{coarse} = \frac{\Delta x}{L_s} C_e \frac{M^2 H^2}{f}, \quad \text{where } \Delta x > L_s. \quad (3)$$

For conciseness, we denote the tracer, POC, by c . A scaling estimate for the vertical POC flux (Sec. S3.1) $Flux = \langle w'c' \rangle$ must account for the fact that tracer c is not aligned with

the isopycnal surfaces. While the isopycnal surfaces are slanted, the POC gradient is largely vertical. Therefore,

$$\langle w'c' \rangle \sim \psi_e \frac{|\nabla b|}{b_z} \langle c_z \rangle = \psi_e \Gamma \langle c_z \rangle = C_e \frac{M^4 H^2 [POC]}{N^2 f H^*}. \quad (4)$$

Here $\Gamma = \frac{|\nabla b|}{b_z}$ is the isopycnal slope. The vertical POC gradient $\langle c_z \rangle$ is evaluated as $\langle c_z \rangle = [POC]/H^*$, where $[POC]$ is the surface POC, and H is the depth of the photosynthetically productive layer that is POC-rich. In the subpolar oceans during spring, the ML depth H is an appropriate choice for H^* , whereas in other regions (as later shown), the euphotic depth is a better choice for H^* . This scaling estimate is based on area-averaged (or strictly speaking, frontally averaged) quantities, denoted by $\langle \rangle$, $[\]$.

S3.3.1 Testing the scaling for the POC flux against model simulations

We test the parameterization (4) against our process study model simulations (Fig. 4a) in which we resolve the eddy-driven flux of POC, $\langle w'c' \rangle$. All the parameters in the scaling estimate (4) and in ψ_e (2) are evaluated as spatial averages from the model solution as a function of time. We computed the surface $[POC]$ as the vertically averaged POC over the upper 50 m at each time step of the model. We estimate the average ML depth H using a density criterion of 0.05 from 10 m, and choose $H^* = 175$ (Fig S13a). We evaluate the lateral buoyancy gradient $M^2 = |\nabla b|$ and the buoyancy frequency $N^2 = b_z$, vertically averaged over the upper 50 m at each time step of the model. While $[POC]/H^*$ increases with time (solid line, Fig. S14a), the isopycnal slope Γ decreases (dashed line), as does the eddy overturning streamfunction ψ_e (dotted line). Consistent with these trends, the parameter $\frac{M^4}{(Nf)^2}$ becomes $\ll 1$ as stratification intensifies due to the slumping caused by eddies. The stratification N^2 formed in this way far exceeded what would be expected of an equilibrated front, for which the scaling is $N^2 f^2 \sim M^4$ (50). A regression of the model-resolved POC flux $F_{100} = \langle w'c' \rangle$ at 100 m depth, with the model-derived scaling estimate $C_e [POC] \frac{M^4 H}{N^2 f}$, is shown in Fig. S14b. We find that the parameterization of flux (evaluated in the model) is strongly correlated with the spatially averaged, model-resolved flux $\langle w'c' \rangle$ between $z = -80$ to -300 m, with r^2 ranging between 0.88 and 0.5 (Fig. S14c).

S3.3.2 Relationship between the scaling and glider-derived POC flux

The estimate for POC flux derived from the glider observations, $Flux_{obs} = [POC]U_s\Gamma$ is consistent with the scaling derived above. Since the glider-derived U_s can be scaled, using thermal wind balance as $U_s/H \sim M^2/f$, we get $Flux_{obs} = [POC] \frac{HM^2}{f} \frac{M^2}{N^2}$.

S3.4 Estimating the global eddy-driven POC flux

The scaling estimate for the eddy driven POC flux can serve as a parameterization and be used to assess the contribution of the mechanism globally. To obtain a global estimate of the

springtime POC export through eddy-driven subduction evaluate the scaling estimate (4) using global datasets to determine the value of the parameters H , M^2 , N^2 and $\langle \frac{\partial POC}{\partial z} \rangle$. Since we use gridded data, we use (3) to evaluate ψ_e^{coarse} in place of ψ_e .

We use climatological datasets to evaluate the parameters in the scaling over springtime, by time-averaging March, April, and May in the Northern hemisphere and Sep, Oct, Nov in the Southern hemisphere. The surface POC concentration (Fig. S15a) is derived from level 3 gridded POC from SeaWIFS (<http://oceancolor.gsfc.nasa.gov/>) and interpolated on to the $0.5^\circ \times 0.5^\circ$ grid of the MIMOC database. The other parameters, M^2 , N^2 , H are calculated from the Monthly Isopycnal and Mixed layer Climatology (MIMOC, <http://www.pmel.noaa.gov/mimoc/>). The mixed layer depth H (Fig. S15b) is calculated by finding the depth at which the density differs by 0.05 kg m^{-3} from the surface bin. The buoyancy frequency (N^2 , Fig. S15c) is calculated by differencing the density at 5 m vertical bins, and then averaging over the depth of the wintertime mixed layer at each grid cell. The lateral buoyancy gradient (M^2 , Fig. S15d) is evaluated using the first order difference for the gradient (using both zonal and meridional components) at a depth of 10 m over the $0.5^\circ \times 0.5^\circ$ grid of the MIMOC database. To account for the under-representation of the lateral buoyancy gradient due to the spatial resolution of the dataset, we use the pre-factor $\Delta x/L_s$ in (3) as suggested by Fox-Kemper et al. (49), where the frontal length scale $L_s = 4 \text{ km}$, the grid scale $\Delta x = 0.5^\circ$ (converted to km), and a transfer efficiency $C_e = 0.08$ consistent with (29).

S3.4.1 Evaluating biases and uncertainties in the parameters for the global flux estimate

Uncertainties in several factors can bias our global estimate for the eddy-driven subduction of POC.

- *Timing of the spring bloom:* We evaluate the subduction during the spring season, for which we use the monthly climatologies of Mar-Apr-May in the northern hemisphere, and Sep-Oct-Nov in the southern hemisphere. But the maximum transition in the mixed layer may occur in different months (whereas we use the 3 month period). We examined the month of maximum transition in the MIMOC climatology, but found that this had reasonably poor spatial coherence. Thus, when we evaluated the global POC scaling specifically at the 'transition month' it introduced noisiness at small-scales into our maps of the flux, and we did not feel that this improved the estimate.
- *Depth over which N^2 is evaluated:* The depth over which seasonal restratification occurs varies widely across the globe. Choosing a fixed depth over which to evaluate N^2 in the flux scaling (as we did in the NAB08 region) would result in biases when applied globally. Therefore, at each grid cell, we evaluate N^2 over the depth of the climatological deepest winter mixed layer at that location. This way, we ensure that N^2 is evaluated over the mixed layer and the restratified pycnocline beneath.
- *Evaluating the vertical gradient in POC:* In the subtropical and tropical regions, the depth of the euphotic layer (defined as the 1% light level) exceeds the mixed layer depth

(Fig. S16a). These regions experience less of a seasonal (springtime) transition in the mixed layer depth and the production of phytoplankton tends to be limited more by nutrients than light. In the global scaling, we approximate the vertical gradient of POC as $[POC]/H^*$ where $[POC]$ is the surface concentration, and we assume that the POC goes to zero at H^* . Using $H^* = H$, the ML depth, in the NAB08 region worked well because in spring, phytoplankton growth is light-limited, and the POC concentration tends to become negligible near the ML base. However in other regions, particularly where mixed layers are shallow even during spring and light penetrates deeper than the ML, POC is non-zero at the ML base, and H^* is most appropriately defined as the depth of euphotic layer z_{eu} , where light reaches 1% of its surface value. Therefore, we define H^* (Fig. S16b) as

$$H^* = \max(H, |z_{eu}|) \quad (5)$$

We test our assumption that $[POC]/H^*$ describes the surface POC gradient ($(\frac{\partial POC}{\partial z})$) at three locations where we have vertically-resolved data of the POC distributions: the NAB08 site, the Bermuda Atlantic Timeseries Station (BATS) and the Hawaiian Ocean Timeseries (HOT). At each location, we evaluate the mixed layer depth from CTD profiles (based on a 0.05 density criterion relative to 10 m depth, black line, Fig. S17a-f). A depth-resolved timeseries of POC at NAB08 was derived from a calibrated beam transmissivity proxy (Fig. S17d), and from filtered bottle samples at discrete depths at BATS and HOT (Fig. S17e,f). The “true” POC gradient $\frac{\partial POC}{\partial z}$ is obtained from each profile as the slope of the linear fit of POC with depth, evaluated between the surface and H^* . We compare this to our bulk estimate for the gradient $[POC]/H^*$ where $[POC]$ is the concentration at 10 m depth. A regression of the resolved (or “true”) POC gradient with the bulk estimate yields a significant correlation in each case ($r^2 = 0.40, 0.61$ and 0.36 respectively), and a high skill, with a slope (black dashed) close to the one-to-one line (red) in each case. These results suggest that approximating the vertical gradient in POC by $[POC]/H^*$ is a reasonable first-order approach. Global depth-resolved observations of POC (such as those that will be provided through the Bio-ARGO program) will help to further evaluate this approximation.

S3.4.2 Global estimation of eddy-driven POC flux and comparison with sinking POC export

The global map of springtime eddy-driven subduction is shown in Fig. S18a. We find that localized eddy-export of POC may contribute between 1 and 100 $\text{mgC m}^{-2} \text{d}^{-1}$ depending on region, and roughly 50 $\text{mgC m}^{-2} \text{d}^{-1}$ in the NAB08 region at 60° N. This parameterization represents a temporal and spatial average over the patch scales and bloom events (described in Table S1) and therefore, it is not surprising that it generally has a lower magnitude.

We compare the POC export by eddy-driven subduction with that from sinking particles in Fig. S18b. The sinking export flux s derived by Siegel et al. (33) from satellite- and model-based estimates at the base of the euphotic layer. In the estimate of sinking flux too, we see

lower export values (roughly $100 \text{ mgC m}^{-2} \text{ d}^{-1}$) for the spring season in comparison with the in situ estimates obtained from NAB08 (Table S1) for the reasons discussed above. The sinking flux estimate is biased low in the Southern Ocean (personal communication, D.A. Siegel).

We add these two export estimates (subduction + sinking) to get a ‘total’ passive POC export, and then examine the percentage of the total contributed by eddy-driven processes (Fig. 4c). In particular, the Southern Ocean, the Kuroshio current and the subpolar North Atlantic stand out, with eddy-driven subduction representing 25% to 60% of the total.

TABLE S1

	$Flux (mgC m^{-2} d^{-1})$	$depth$	$method$	$citation$
Large (sinking) particles and aggregates	514 (NAB08, during diatom event)	100 m	b_{bp} spike analysis	(21)
	150 (NAB08, after diatom event)			
	160 (NAB08, during diatom event)	600 m	sediment trap	(31)
	168 (NABE)	100 m	fit to sediment trap	(51)
	275 (NAB08)	100 m	modeled aggregates, cysts, detritus	(26)
	30 - 100 (climatological)	z_{eu}	satellite observations & ecosystem modeling	(33)
Small particles (weak or no sinking)	50-200 (Bio-ARGO)	100 m	rate of change in b_{bp}	(37)
	108 (NAB08)	100 m	model: contribution by single cells	(26)
	50-160 (NAB08)	100 m	PSOM model	<i>this study</i>
	20-200	100 m	Parameterization based on spring climatology	<i>this study</i>
Total POC export	984 (NAB08, during diatom event)	MLD	$NCP - \frac{\partial POC}{\partial t}$	(23)
	276 (NAB08, before diatom event)			
	620 (NAB08, during diatom event)	100 m	^{234}Th disequilibria	(31)
	20 (NAB08, before diatom event)			
	540 (NAB08)	100 m	coupled biophysical model	(26)

Table S1: A summary of various estimates of POC export during the springtime North Atlantic bloom. The model estimate and global parameterization of eddy-driven export presented here represents spatially-averaged conditions, while NAB08 publications also document the enhanced export that occurred during a short-lived diatom bloom event. Here, we attempt to distinguish the event-based, and mean export estimates.

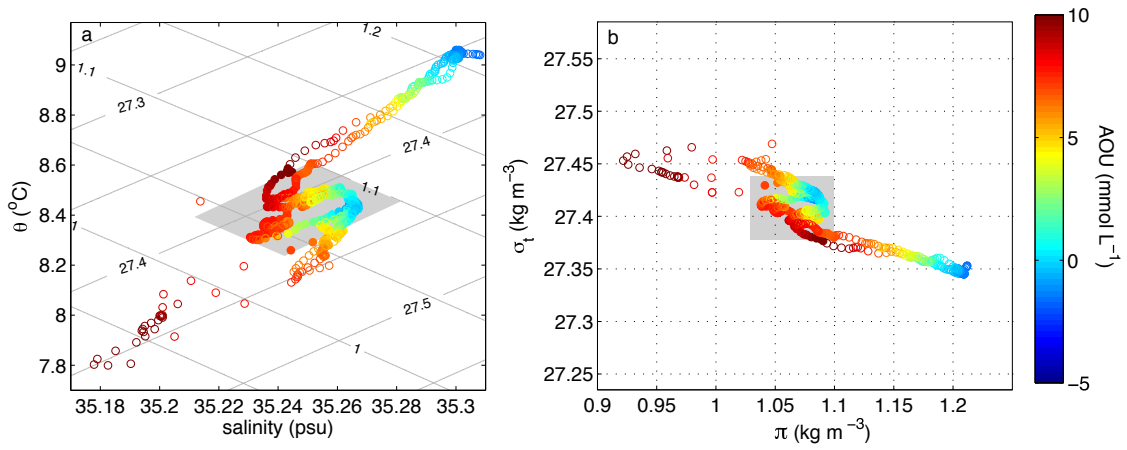


Figure S2: a) Potential temperature (θ) versus salinity, and b) potential density (σ_t) versus spice (π) from the glider profile examples shown in Fig. 1b. Apparent oxygen utilization (AOU) is in colors and the region surrounding the water mass intrusion is indicated by gray shading.

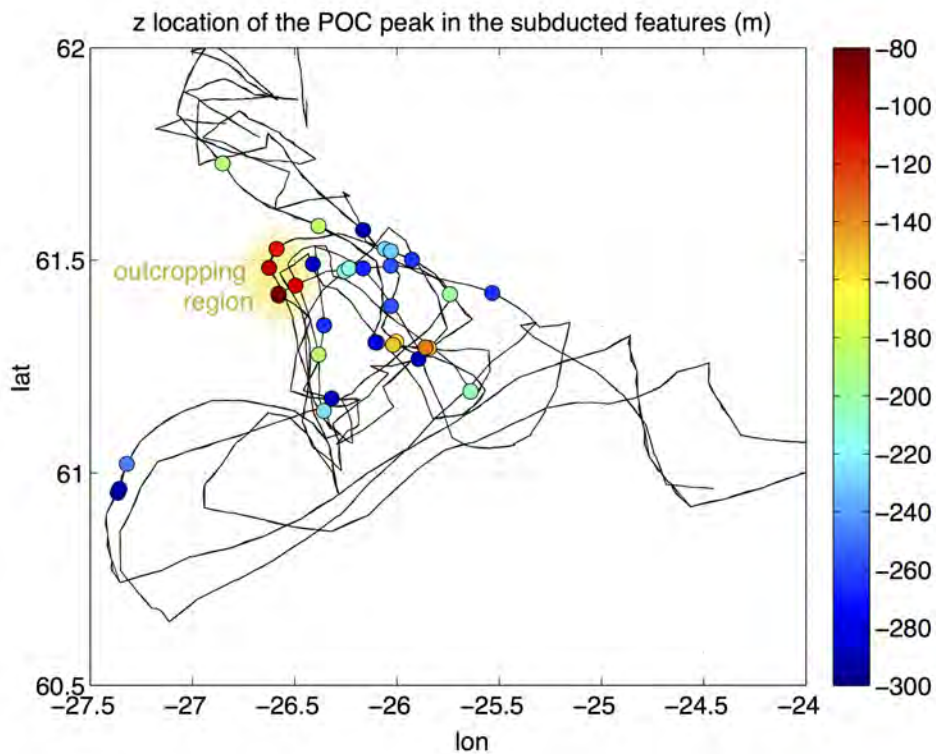


Figure S3: Mean depth of the 33 subsurface features defined by $\sigma_t = 27.48 \pm 0.005 \text{ kg m}^{-3}$ (colored circles) overlaid on the tracks of the Seagliders (black lines). The yellow shading indicates the features whose upper edge outcropped in the mixed layer (see year day 130, Fig. 4c), and were located near the north-west edge of the anticyclone (see Fig. 3e for the dynamic height). These shallow features also contained the maximum POC and DO (not shown) and may represent the source location for the deeper features that were observed later.

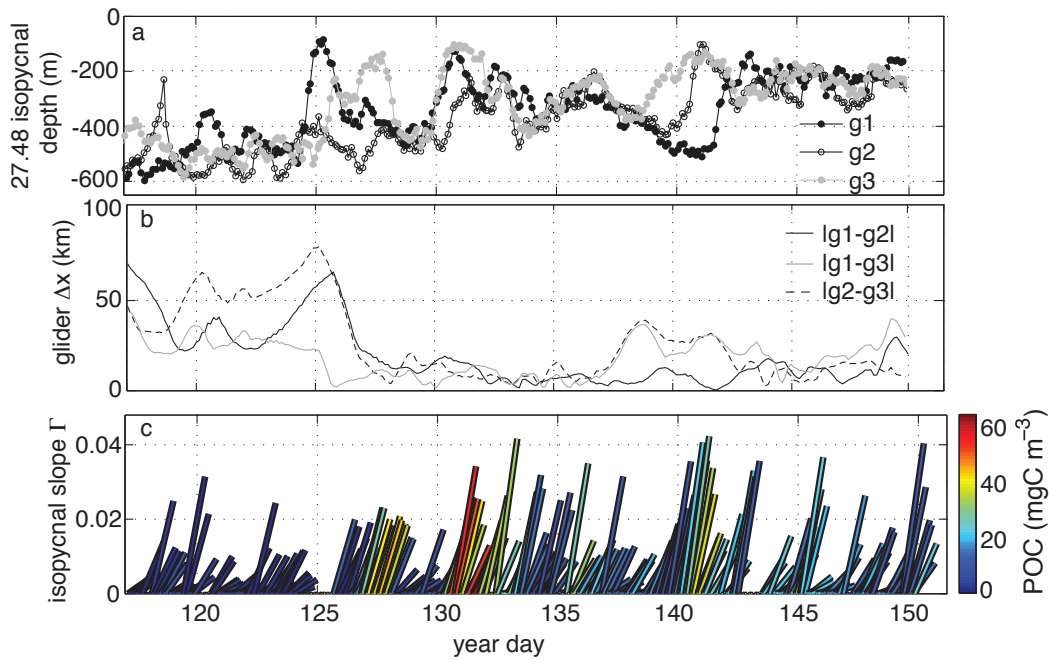


Figure S4: a) Depth of the 27.48 isopycnal from Seaglider 1 (black, filled circles), Seaglider 2 (open circles) and Seaglider 3 (gray circles). b) Horizontal separation between the NAB08 Seagliders 1 and 2 (black solid line), 2 and 3 (black dashed line), 1 and 3 (gray line) versus year day. c) Slope of the 27.48 isopycnal computed by fitting a plane between the isopycnal position at gliders 1, 2, and 3. The slope of the isopycnal is shown by the height and also by the tilt of the bar, where more vertically-tilted bars indicate large isopycnal slopes. Each bar is colored by the mean POC on the 27.48 isopycnal between the three gliders.

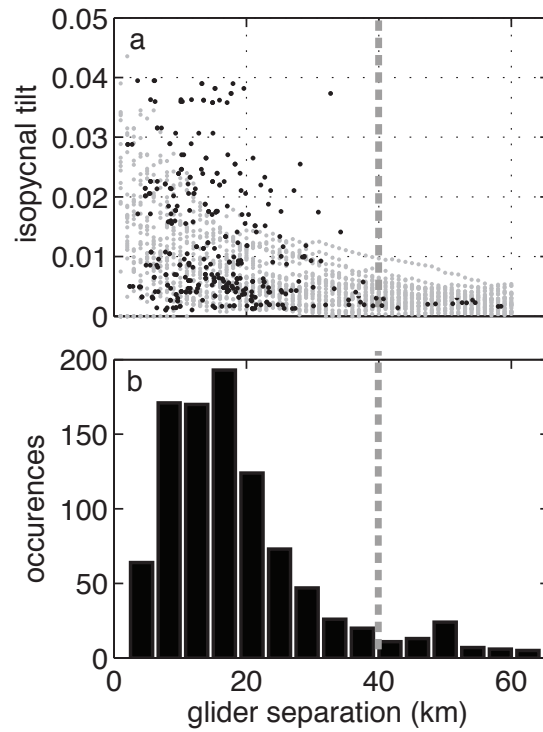


Figure S5: a) Isopycnal tilt versus the mean glider separation from the model (gray points, 1km grid) and the NAB08 Seagliders (black points). (b) A histogram of the Seaglider separations observed between yearday 110 and 150. The gray dashed line indicates the 40 km cut-off for the maximum allowable mean separation distance of the three gliders.

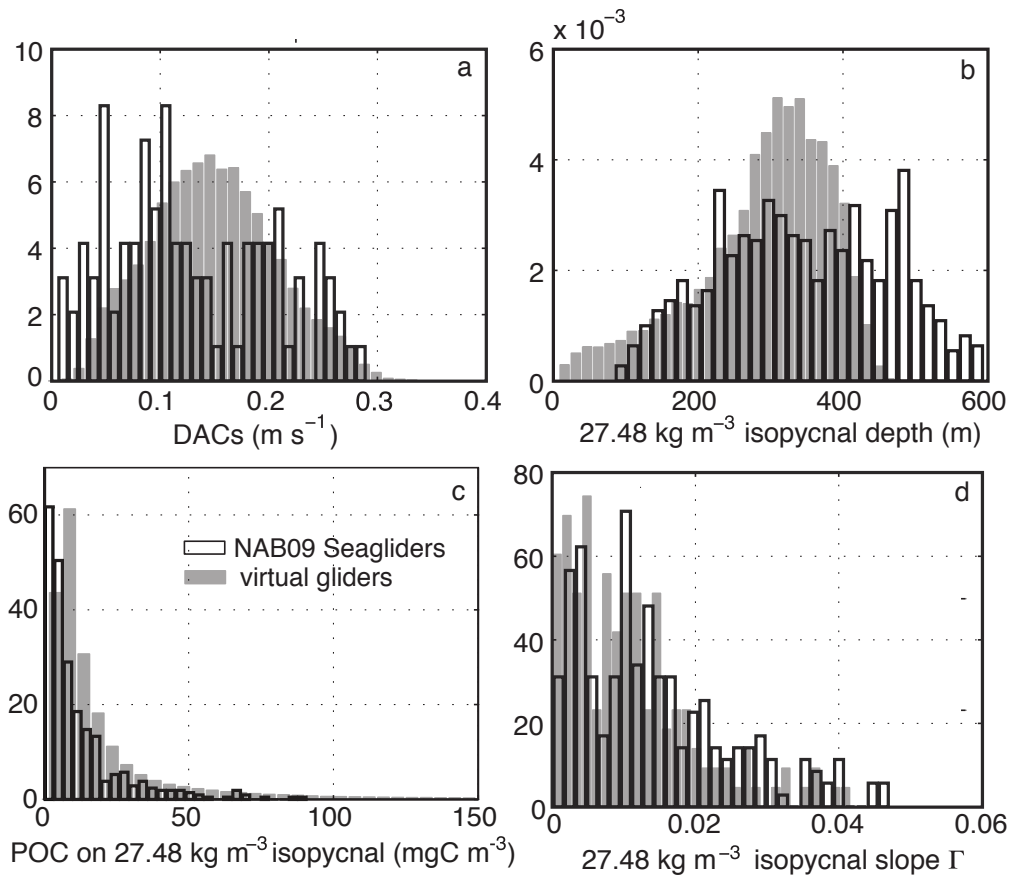


Figure S6: Histograms of (a) Depth averaged currents, DACs, (b) the 27.48 isopycnal depth, (c) POC on the 27.48 isopycnal, (d) 27.48 isopycnal slope (Γ) computed from near-simultaneous observations from three gliders within <40 km radius of each other.

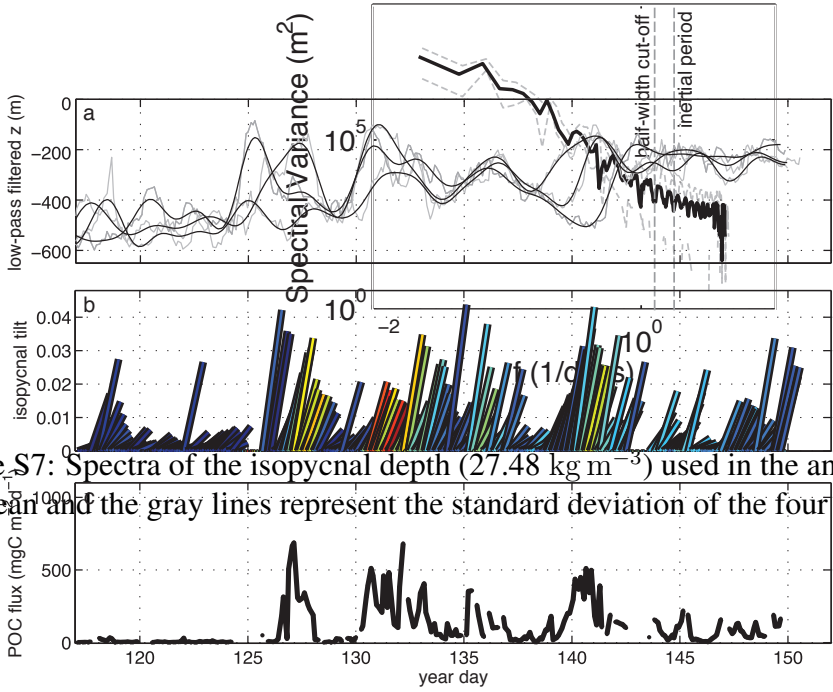


Figure S7: Spectra of the isopycnal depth (27.48 kg m^{-3}) used in the analysis. The solid line is the mean and the gray lines represent the standard deviation of the four glider time series.

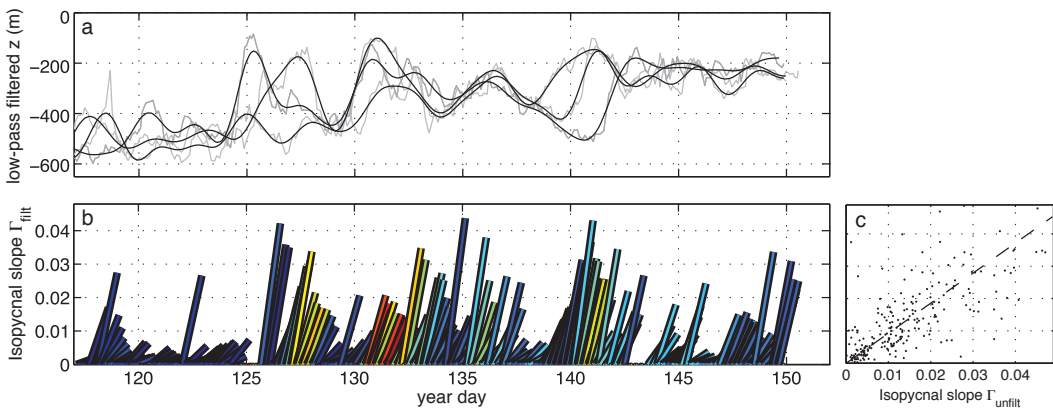


Figure S8: a) Low-pass filtered (black lines) and unfiltered (gray lines) isopycnal depth. These were filtered with a PL64 filter that removed the near-internal, tidal and high frequency components of the internal wave spectrum. b) Slope of the 27.48 isopycnal (following Fig. S7c), computed using the filtered isopycnal depths. c) scatter plot of the filtered versus unfiltered isopycnal slopes, with a slope of 0.91 and an r^2 of 0.51 .

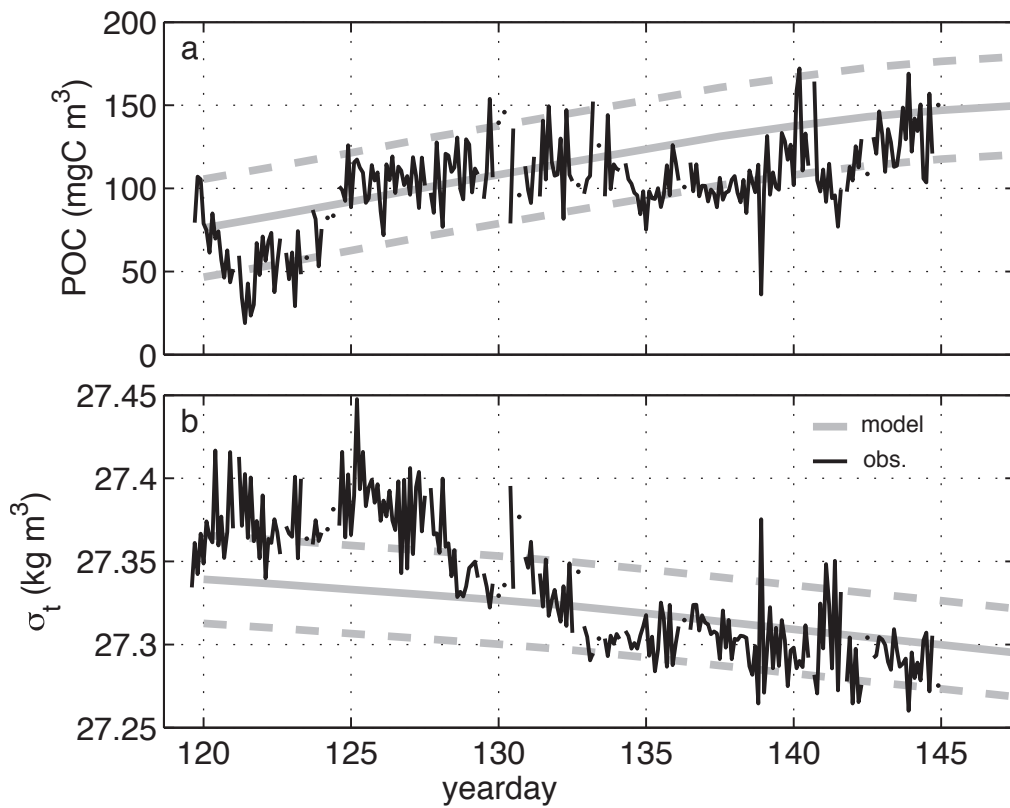
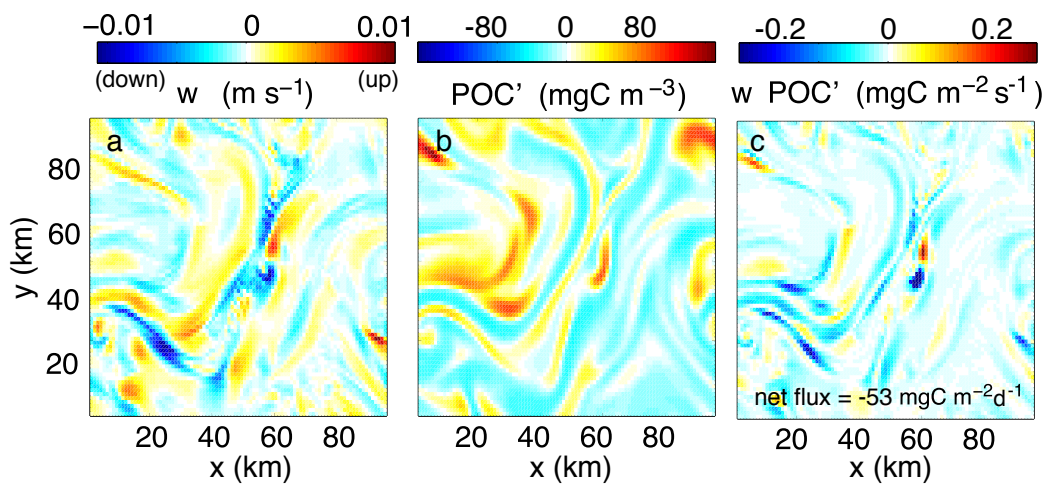
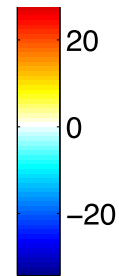


Figure S9: Timeseries of a) POC and b) potential density (σ_t) averaged over the upper 50 m in and amongst the four Seagliders (black) and spatially averaged over the upper 50 m in the model (gray). The dashed gray lines indicate the standard deviation due to horizontal variability in the model.

wards = red

$\lambda, \lambda = -69.0021 \text{ m}$

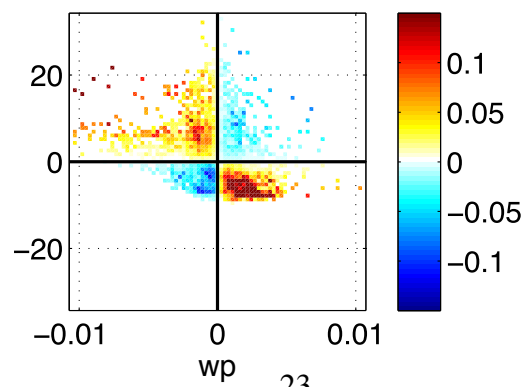
TRp (mgC m^{-3})



.05

Figure S10: (a) Model vertical velocity (w'), (b) POC anomaly (c'), and (c) the product $w'c'$ at the 100 m depth bin on year day 140. Negative (blue color) in (c) indicates a downward flux of POC.

0.05



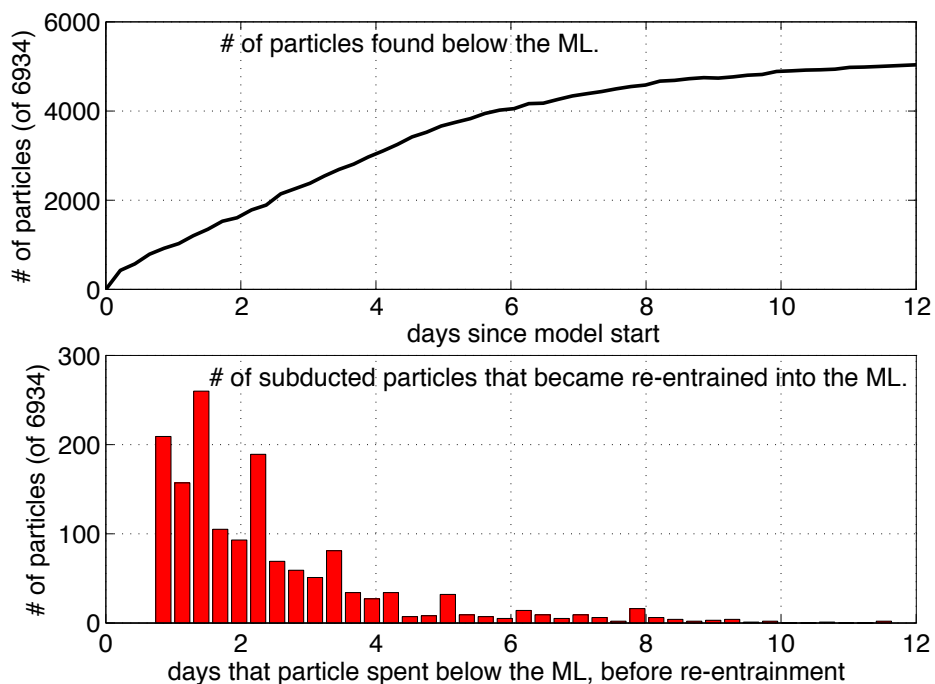


Figure S11: a) Timeseries of the number of modeled particles that were found below the mixed layer at the x-y location corresponding to the particle. Initially, all of the particles were within the mixed layer. After 12 days, 72% of the particles (5006 of 6934) had been subducted below the mixed layer. b) 22% of the particles that were subducted were re-entrained into the mixed layer at some point. The histogram indicates the number of days that these particles spent below the mixed layer before re-entrainment.

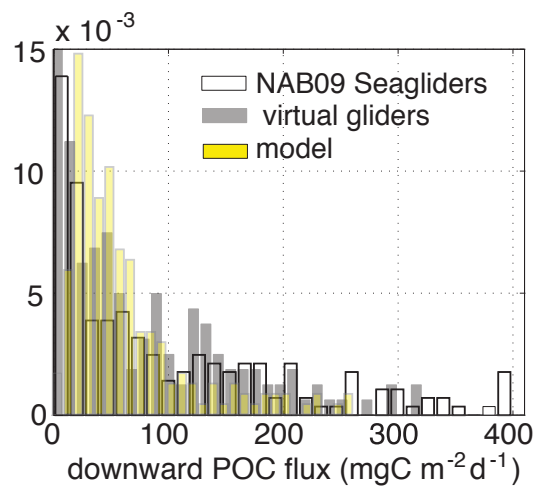


Figure S12: Histogram of various vertical POC flux estimates. Distributions are shown from the NAB08 Seaglider analysis (white bars), and from applying the identical analysis to virtual gliders planted in the model, with the same trajectories as the NAB08 gliders (gray bars). In panel (e), the yellow bars show the distribution of flux values between 100 and 250 m obtained from $\langle w'POC' \rangle$, for comparison with the glider-based estimates (white and gray bars).

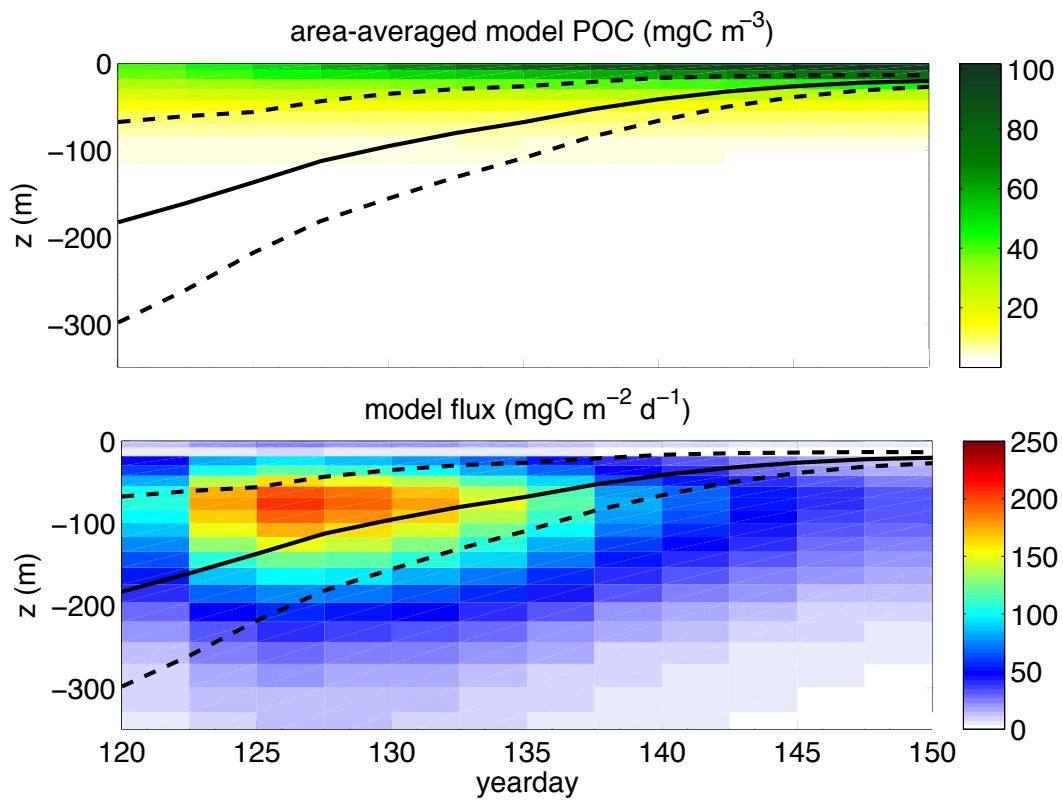


Figure S13: a) Depth-resolved, horizontally-averaged model POC, and b) model-based POC flux $\langle w'c' \rangle$. The solid black line is the mean MLD, and the dashed lines indicate the standard deviation in MLD. Notice that the variability in MLD is initially high, and decreases as restratification progresses.

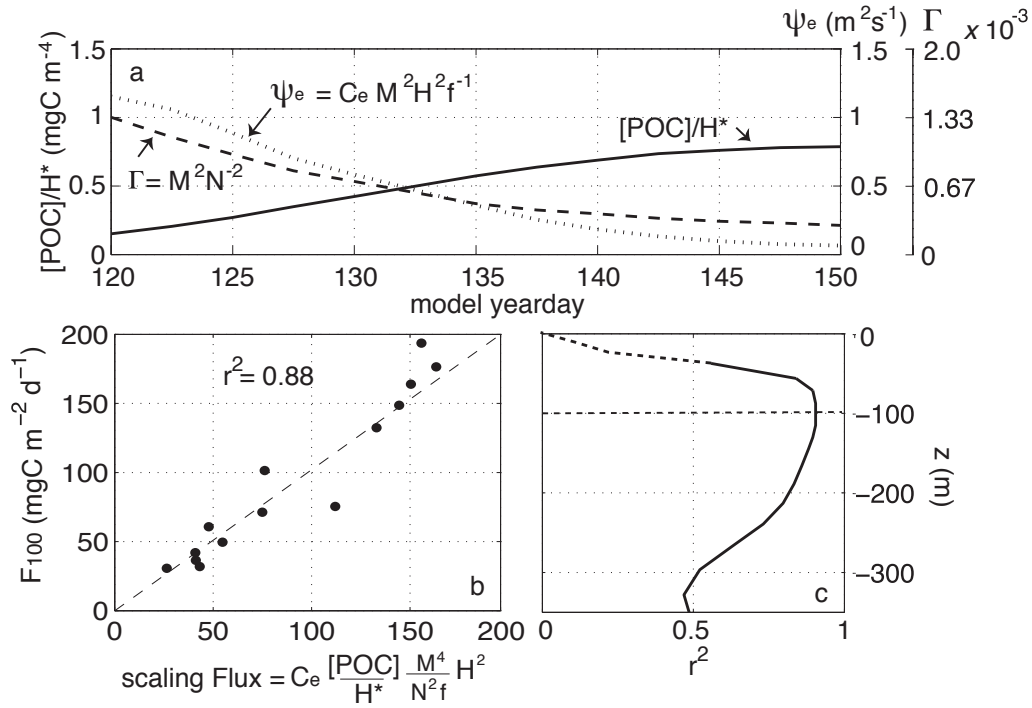


Figure S14: (a) Timeseries of approximate POC gradient $[POC]/H^*$ (solid line), Γ (dashed line) and ψ_e (dotted line) derived from M^2 , N^2 and POC averaged over the upper 50 m and horizontally over the domain. H^* is the length scale over which the POC approaches zero (see section S3.4.1). (b) A regression of the model-based flux $\langle w'c' \rangle$ at 100 m (F_{100}) with the flux scaling. (c) The correlation coefficient (r^2) between the model-based flux (depth-resolved) and the flux scaling. The solid line indicates a significant ($n \ll 0.001$), positive correlation.

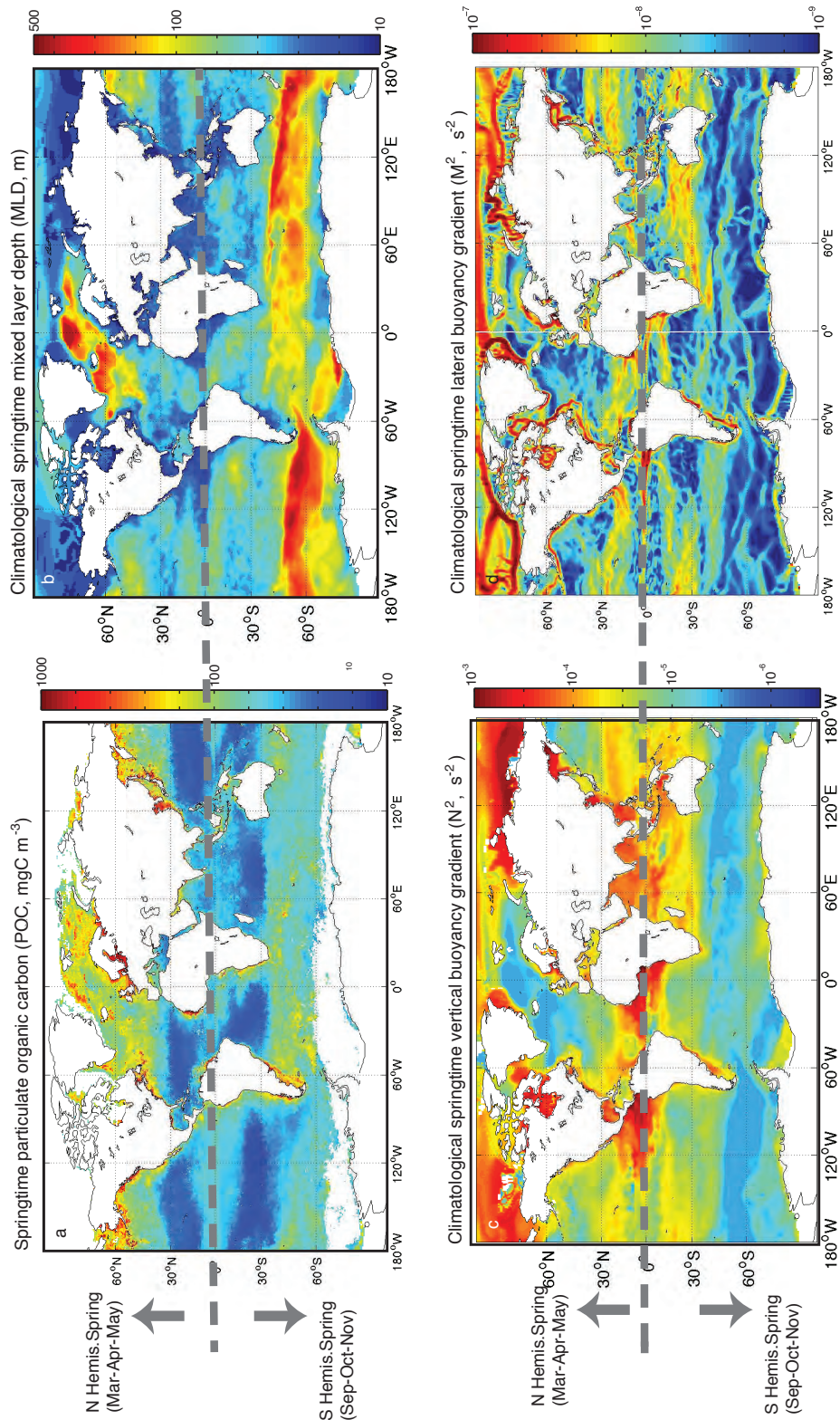


Figure S15: Climatological springtime a) surface POC (level 3 gridded SeaWiFS), b) ML depth H , c) buoyancy frequency (N^2) and c) lateral buoyancy gradient (M^2) from MIMOC ($0.5 \times 0.5^\circ$). M^2 was computed at the 10 m bin. N^2 was computed over the climatological deepest winter mixed layer depth; the region that becomes stratified in the spring.

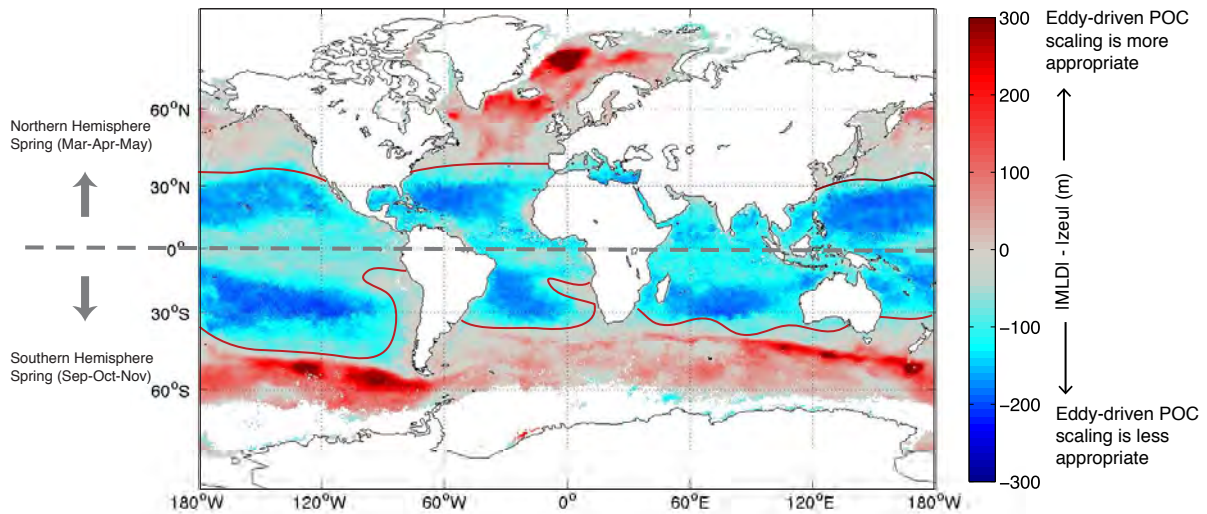


Figure S16: a) Global springtime difference (in m) between the climatological mixed layer depth H (Fig. S15b) and the climatological euphotic depth (z_{eu}) calculated from Level 3 binned SeaWiFS data. Eddy-driven subduction has the greatest impact on POC export in regions where $H > |z_{eu}|$. b) Length scale H^* (m) which is the deeper of MLD or z_{eu} . This length scale represents the scale over which we assume that there is a POC gradient acted upon by eddy subduction such that $\frac{\partial POC}{\partial z} \sim \frac{POC_{surface}}{H^*}$.

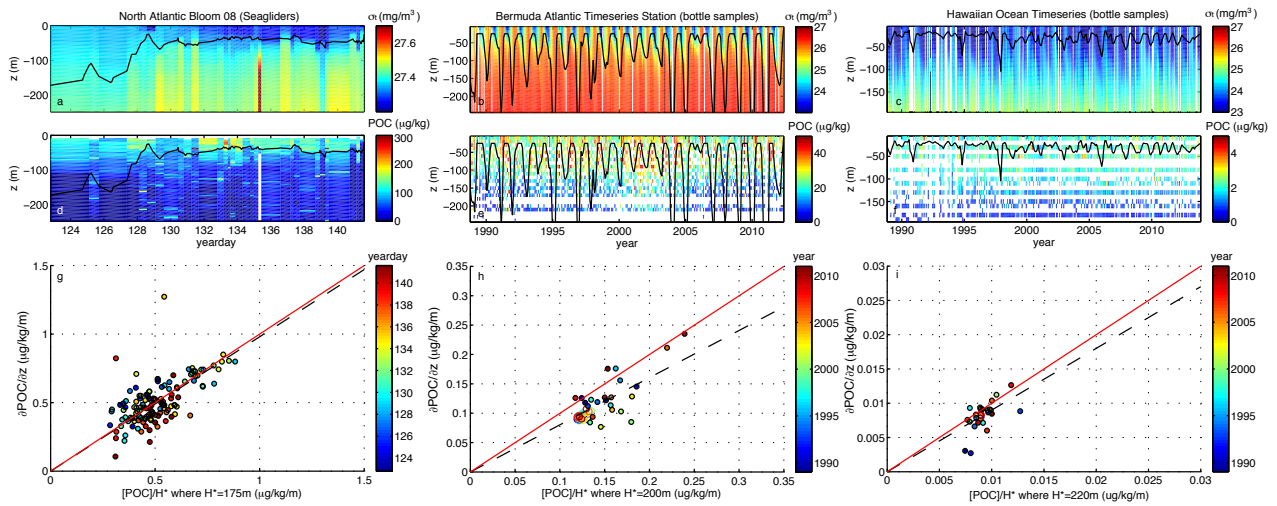


Figure S17: A test of the vertical POC gradient scaling. Timeseries of density (σ_t) from ship-based profiles a) during the NAB08 experiment, b) at the Bermuda Atlantic Timeseries Station (BATS) and c) at the Hawaiian Ocean Timeseries site (HOT). The black line in each case is the mixed layer depth defined with a density criterion of 0.05 kg m^{-3} . Timeseries of POC measured from d) the calibrated beam transmissometer at NAB08, and filtered water samples at e) BATS and f) HOT. The vertical gradient of POC was estimated by finding the slope of the 'best fit' line (minimizing rms error) which gave $\partial\text{POC}/\partial z$, versus the scaling argument the surface $[\text{POC}]/H^*$ (see figure S17b). The correlation is significant ($r^2=0.40$, 0.61 and 0.36 respectively) and the slope (black dashed) is near one (red line) (slope = 0.98 ± 0.29 , 0.80 ± 0.26 and 0.90 ± 0.17 respectively). In h) and i), the open circles represent winter-time conditions (DJF) and the filled circles represent spring conditions (MAM).

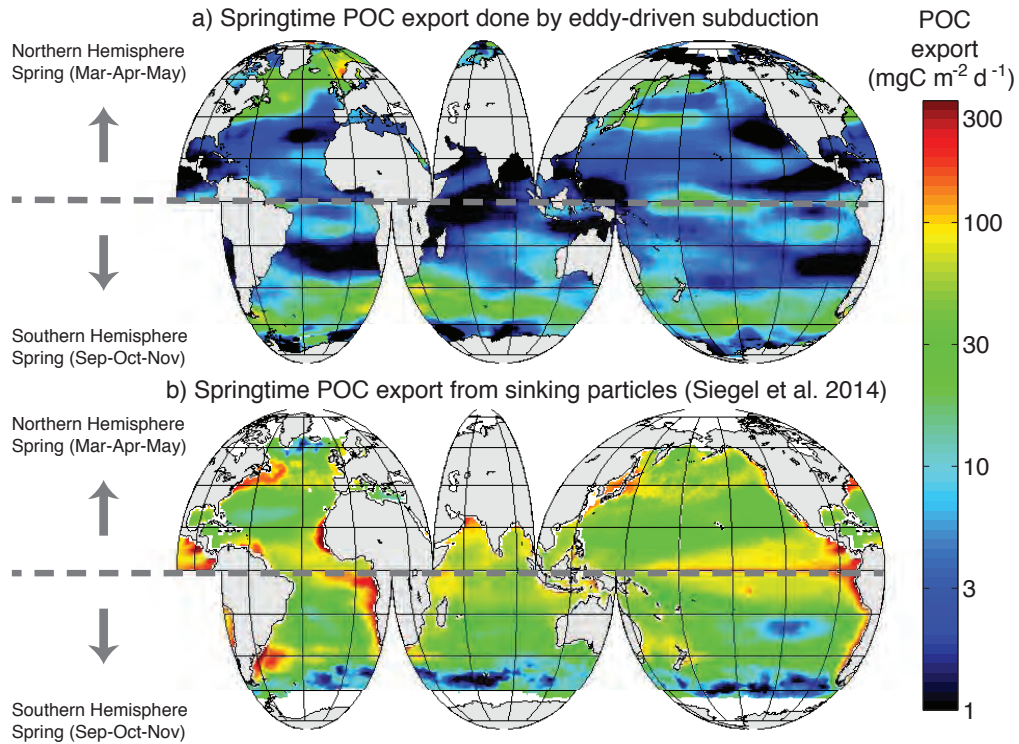


Figure S18: Global springtime climatological estimates of a) export done by eddy-driven subduction, based on the parameterization described here. The red line indicates the boundary within which the springtime euphotic depth z_{eu} (computed from level 3 gridded SeaWiFS) is deeper than the mixed layer depth (computed from MIMOC climatology, with a 0.05 kg m^{-3} density criteria). See Fig. S13. In these regions we scale the POC gradient by $H^*=z_{eu}$ (see section S3.4.1). b) Export at the euphotic base by sinking particles, from Siegel et al. 2014. The red line indicates the boundary of the high-nutrient low-chl (HNLC) regions of the Southern Ocean which may be underestimated in their model.

References

1. R. Sanders, S. A. Henson, M. Koski, C. L. De La Rocha, S. C. Painter, A. J. Poulton, J. Riley, B. Salihoglu, A. Visser, A. Yool, R. Bellerby, A. P. Martin, The biological carbon pump in the North Atlantic. *Prog. Oceanogr.* **129**, 200–218 (2014). [doi:10.1016/j.pocean.2014.05.005](https://doi.org/10.1016/j.pocean.2014.05.005)
2. A. Körtzinger, U. Send, R. S. Lampitt, S. Hartman, D. W. R. Wallace, J. Karstensen, M. G. Villagarcia, O. Llinás, M. D. DeGrandpre, The seasonal $p\text{CO}_2$ cycle at 49°N/16.5°W in the northeastern Atlantic Ocean and what it tells us about biological productivity. *J. Geophys. Res.* **113** (C4), C04020 (2008). [doi:10.1029/2007JC004347](https://doi.org/10.1029/2007JC004347)
3. C. L. Sabine, R. A. Feely, N. Gruber, R. M. Key, K. Lee, J. L. Bullister, R. Wanninkhof, C. S. Wong, D. W. Wallace, B. Tilbrook, F. J. Millero, T. H. Peng, A. Kozyr, T. Ono, A. F. Rios, The oceanic sink for anthropogenic CO₂. *Science* **305**, 367–371 (2004). [Medline doi:10.1126/science.1097403](https://doi.org/10.1126/science.1097403)
4. M. J. Follows, R. G. Williams, J. C. Marshall, The solubility pump of carbon in the subtropical gyre of the North Atlantic. *J. Mar. Res.* **54**, 605–630 (1996). [doi:10.1357/0022240963213682](https://doi.org/10.1357/0022240963213682)
5. W. D. Gardner, S. P. Chung, M. J. Richardson, I. D. Walsh, The oceanic mixed-layer pump. *Deep Sea Res. Part II Top. Stud. Oceanogr.* **42**, 757–775 (1995). [doi:10.1016/0967-0645\(95\)00037-Q](https://doi.org/10.1016/0967-0645(95)00037-Q)
6. H. U. Sverdrup, On conditions for the vernal blooming of phytoplankton. *Journal du Conseil International pour l'Exploration de la Mer* **18**, 287–295 (1953). [doi:10.1093/icesjms/18.3.287](https://doi.org/10.1093/icesjms/18.3.287)
7. A. Mahadevan, E. D'Asaro, C. Lee, M. J. Perry, Eddy-driven stratification initiates North Atlantic spring phytoplankton blooms. *Science* **337**, 54–58 (2012). [Medline doi:10.1126/science.1218740](https://doi.org/10.1126/science.1218740)
8. J. Taylor, R. Ferrari, Shutdown of turbulent convection as a new criterion for the onset of spring phytoplankton blooms. *Limnol. Oceanogr.* **56**, 2293–2307 (2011). [doi:10.4319/lo.2011.56.6.2293](https://doi.org/10.4319/lo.2011.56.6.2293)
9. H. W. Ducklow, R. P. Harris, Introduction to the JGOFS North Atlantic bloom experiment. *Deep Sea Res. Part II Top. Stud. Oceanogr.* **40**, 1–8 (1993). [doi:10.1016/0967-0645\(93\)90003-6](https://doi.org/10.1016/0967-0645(93)90003-6)
10. J. B. Sallée, R. J. Matear, S. R. Rintoul, A. Lenton, Localized subduction of anthropogenic carbon dioxide in the Southern Hemisphere oceans. *Nat. Geosci.* **5**, 579–584 (2012). [doi:10.1038/ngeo1523](https://doi.org/10.1038/ngeo1523)
11. J. A. Barth, Injection of carbon from the shelf to offshore beneath the euphotic zone in the California Current. *J. Geophys. Res.* **107** (C6), 3057 (2002). [doi:10.1029/2001JC000956](https://doi.org/10.1029/2001JC000956)
12. P. Karleskind, M. Lévy, L. Memery, Subduction of carbon, nitrogen, and oxygen in the northeast Atlantic. *J. Geophys. Res.* **116** (C2), C02025 (2011). [doi:10.1029/2010JC006446](https://doi.org/10.1029/2010JC006446)

13. A. Mahadevan, Modeling vertical motion at ocean fronts: Are nonhydrostatic effects relevant at submesoscales? *Ocean Model.* **14**, 222–240 (2006). [doi:10.1016/j.ocemod.2006.05.005](https://doi.org/10.1016/j.ocemod.2006.05.005)
14. A. Mahadevan, A. Tandon, An analysis of mechanisms for submesoscale vertical motion at ocean fronts. *Ocean Model.* **14**, 241–256 (2006). [doi:10.1016/j.ocemod.2006.05.006](https://doi.org/10.1016/j.ocemod.2006.05.006)
15. M. A. Spall, Frontogenesis, subduction, and cross-front exchange at upper ocean fronts. *J. Geophys. Res.* **100** (C2), 2543–2557 (1995). [doi:10.1029/94JC02860](https://doi.org/10.1029/94JC02860)
16. M. Lee, A. Nurser, eddy subduction and the vertical transport streamfunction. *J. Phys. Oceanogr.* **42**, 1762–1780 (2012). [doi:10.1175/JPO-D-11-0219.1](https://doi.org/10.1175/JPO-D-11-0219.1)
17. J. C. McWilliams, F. Colas, M. J. Molemaker, Cold filamentary intensification and oceanic surface convergence lines. *Geophys. Res. Lett.* **36**, L18602 (2009). [doi:10.1029/2009GL039402](https://doi.org/10.1029/2009GL039402)
18. M. Lévy, P. Klein, A. M. Treguier, Impact of sub-mesoscale physics on production and subduction of phytoplankton in an oligotrophic regime. *J. Mar. Res.* **59**, 535–565 (2001). [doi:10.1357/002224001762842181](https://doi.org/10.1357/002224001762842181)
19. R. Pollard, L. Regier, Large variations in potential vorticity at small spatial scales in the upper ocean. *Nature* **348**, 227–229 (1990). [doi:10.1038/348227a0](https://doi.org/10.1038/348227a0)
20. S. Fielding, N. Crisp, J. T. Allen, M. C. Hartman, B. Rabe, H. S. J. Roe, Mesoscale subduction at the Almeria-Oran front. *J. Mar. Syst.* **30**, 287–304 (2001). [doi:10.1016/S0924-7963\(01\)00063-X](https://doi.org/10.1016/S0924-7963(01)00063-X)
21. N. Briggs, M. J. Perry, I. Cetinić, C. Lee, E. D’Asaro, A. M. Gray, E. Rehm, High-resolution observations of aggregate flux during a sub-polar North Atlantic spring bloom. *Deep Sea Res. Part I Oceanogr. Res. Pap.* **58**, 1031–1039 (2011). [doi:10.1016/j.dsr.2011.07.007](https://doi.org/10.1016/j.dsr.2011.07.007)
22. T. Rynearson, K. Richardson, R. S. Lampitt, M. E. Sieracki, A. J. Poulton, M. M. Lyngsgaard, M. J. Perry, Major contribution of diatom resting spores to vertical flux in the sub-polar North Atlantic. *Deep Sea Res. Part I Oceanogr. Res. Pap.* **82**, 60–71 (2013). [doi:10.1016/j.dsr.2013.07.013](https://doi.org/10.1016/j.dsr.2013.07.013)
23. M. B. Alkire, E. D’Asaro, C. Lee, M. Jane Perry, A. Gray, I. Cetinić, N. Briggs, E. Rehm, E. Kallin, J. Kaiser, A. González-Posada, Estimates of net community production and export using high-resolution, Lagrangian measurements of O₂, NO₃⁻, and POC through the evolution of a spring diatom bloom in the North Atlantic. *Deep Sea Res. Part I Oceanogr. Res. Pap.* **64**, 157–174 (2012). [doi:10.1016/j.dsr.2012.01.012](https://doi.org/10.1016/j.dsr.2012.01.012)
24. J. B. Palter, M. S. Lozier, R. T. Barber, The effect of advection on the nutrient reservoir in the North Atlantic subtropical gyre. *Nature* **437**, 687–692 (2005). [Medline doi:10.1038/nature03969](https://doi.org/10.1038/nature03969)
25. A. Mahadevan, J. Oliger, R. Street, A nonhydrostatic mesoscale ocean model. Part I: Well-posedness and scaling. *J. Phys. Oceanogr.* **26**, 1868–1880 (1996). [doi:10.1175/1520-0485\(1996\)026<1868:ANMOMP>2.0.CO;2](https://doi.org/10.1175/1520-0485(1996)026<1868:ANMOMP>2.0.CO;2)
26. W. Bagniewski, K. Fennel, M. J. Perry, E. A. D’Asaro, Optimizing models of the North Atlantic spring bloom using physical, chemical and bio-optical observations from a Lagrangian float. *Biogeosciences* **8**, 1291–1307 (2011). [doi:10.5194/bg-8-1291-2011](https://doi.org/10.5194/bg-8-1291-2011)

27. T. Johnston, O. Cheriton, J. T. Pennington, F. P. Chavez, Thin phytoplankton layer formation at eddies, filaments, and fronts in a coastal upwelling zone. *Deep Sea Res. Part II Top. Stud. Oceanogr.* **56**, 246–259 (2009). [doi:10.1016/j.dsr2.2008.08.006](https://doi.org/10.1016/j.dsr2.2008.08.006)
28. I. Held, T. Schneider, The surface branch of the zonally averaged mass transport circulation in the troposphere. *J. Atmos. Sci.* **56**, 1688–1697 (1999). [doi:10.1175/1520-0469\(1999\)056<1688:TSBOTZ>2.0.CO;2](https://doi.org/10.1175/1520-0469(1999)056<1688:TSBOTZ>2.0.CO;2)
29. B. Fox-Kemper, R. Ferrari, R. Hallberg, Parameterization of mixed layer eddies. Part I: Theory and diagnosis. *J. Phys. Oceanogr.* **38**, 1145–1165 (2008). [doi:10.1175/2007JPO3792.1](https://doi.org/10.1175/2007JPO3792.1)
30. A. Mahadevan, A. Tandon, R. Ferrari, Rapid changes in mixed layer stratification driven by submesoscale instabilities and winds. *J. Geophys. Res.* **115** (C3), C03017 (2010). [doi:10.1029/2008JC005203](https://doi.org/10.1029/2008JC005203)
31. P. Martin, R. S. Lampitt, M. Jane Perry, R. Sanders, C. Lee, E. D’Asaro, Export and mesopelagic particle flux during a North Atlantic spring diatom bloom. *Deep Sea Res. Part I Oceanogr. Res. Pap.* **58**, 338–349 (2011). [doi:10.1016/j.dsr.2011.01.006](https://doi.org/10.1016/j.dsr.2011.01.006)
32. K. O. Buesseler, M. P. Bacon, J. K. Cochran, H. D. Livingston, Carbon and nitrogen export during the JGOFS North Atlantic Bloom experiment estimated from ²³⁴Th: ²³⁸U disequilibria. *Deep-Sea Res. A, Oceanogr. Res. Pap.* **39**, 1115–1137 (1992). [doi:10.1016/0198-0149\(92\)90060-7](https://doi.org/10.1016/0198-0149(92)90060-7)
33. D. A. Siegel, K. O. Buesseler, S. C. Doney, S. F. Sailley, M. J. Behrenfeld, P. W. Boyd, Global assessment of ocean carbon export by combining satellite observations and food-web models. *Global Biogeochem. Cycles* **28**, 181–196 (2014). [doi:10.1002/2013GB004743](https://doi.org/10.1002/2013GB004743)
34. D. Steinberg, B. A. S. Van Mooy, K. O. Buesseler, P. W. Boyd, T. Kobari, D. M. Karl, Bacterial vs. zooplankton control of sinking particle flux in the ocean’s twilight zone. *Limnol. Oceanogr.* **53**, 1327–1338 (2008). [doi:10.4319/lo.2008.53.4.1327](https://doi.org/10.4319/lo.2008.53.4.1327)
35. A. Burd, D. A. Hansell, D. K. Steinberg, T. R. Anderson, J. Arístegui, F. Baltar, S. R. Beupré, K. O. Buesseler, F. DeHairs, G. A. Jackson, D. C. Kadko, R. Koppelman, R. S. Lampitt, T. Nagata, T. Reinthaler, C. Robinson, B. H. Robison, C. Tamburini, T. Tanaka, Assessing the apparent imbalance between geochemical and biochemical indicators of meso- and bathypelagic biological activity: What the @\$#! is wrong with present calculations of carbon budgets? *Deep Sea Res. Part II Top. Stud. Oceanogr.* **57**, 1557–1571 (2010). [doi:10.1016/j.dsr2.2010.02.022](https://doi.org/10.1016/j.dsr2.2010.02.022)
36. S. L. Giering, R. Sanders, R. S. Lampitt, T. R. Anderson, C. Tamburini, M. Boutrif, M. V. Zubkov, C. M. Marsay, S. A. Henson, K. Saw, K. Cook, D. J. Mayor, Reconciliation of the carbon budget in the ocean’s twilight zone. *Nature* **507**, 480–483 (2014). [Medline doi:10.1038/nature13123](https://doi.org/10.1038/nature13123)
37. G. Dall’Olmo, K. A. Mork, Carbon export by small particles in the Norwegian Sea. *Geophys. Res. Lett.* **41**, 2921–2927 (2014). [doi:10.1002/2014GL059244](https://doi.org/10.1002/2014GL059244)
38. T. L. Richardson, G. A. Jackson, Small phytoplankton and carbon export from the surface ocean. *Science* **315**, 838–840 (2007). [Medline doi:10.1126/science.1133471](https://doi.org/10.1126/science.1133471)

39. C. C. Eriksen, T. J. Osse, R. D. Light, T. Wen, T. W. Lehman, P. L. Sabin, J. W. Ballard, A. M. Chiodi, Seaglider: A long-range autonomous underwater vehicle for oceanographic research. *IEEE J. Oceanic Eng.* **26**, 424–436 (2001). [doi:10.1109/48.972073](https://doi.org/10.1109/48.972073)
40. I. Cetinić, M. J. Perry, N. T. Briggs, E. Kallin, E. A. D'Asaro, C. M. Lee, Particulate organic carbon and inherent optical properties during 2008 North Atlantic Bloom Experiment. *J. Geophys. Res.* **117** (C6), C06028 (2012). [doi:10.1029/2011JC007771](https://doi.org/10.1029/2011JC007771)
41. F. Bretherton, R. E. Davis, C. B. Fandry, A technique for objective analysis and design of oceanographic experiments. *Deep-Sea Res.* **23**, 559–582 (1976).
42. D. L. Rudnick, R. Ferrari, Compensation of horizontal temperature and salinity gradients in the ocean mixed layer. *Science* **283**, 526–529 (1999). [Medline](https://pubmed.ncbi.nlm.nih.gov/101126/science.283.5401.526/)
[doi:10.1126/science.283.5401.526](https://doi.org/10.1126/science.283.5401.526)
43. B. Hodges, D. Rudnick, Horizontal variability in chlorophyll fluorescence and potential temperature. *Deep Sea Res. Part I Oceanogr. Res. Pap.* **53**, 1460–1482 (2006).
[doi:10.1016/j.dsr.2006.06.006](https://doi.org/10.1016/j.dsr.2006.06.006)
44. P. Flament, A state variable for characterizing water masses and their diffusive stability: Spiciness. *Prog. Oceanogr.* **54**, 493–501 (2002). [doi:10.1016/S0079-6611\(02\)00065-4](https://doi.org/10.1016/S0079-6611(02)00065-4)
45. E. A. D'Asaro, A diapycnal mixing budget on the Oregon shelf. *Limnol. Oceanogr.* **53**, 2137–2150 (2008). [doi:10.4319/lo.2008.53.5_part_2.2137](https://doi.org/10.4319/lo.2008.53.5_part_2.2137)
46. C. N. Flagg, J. A. Vermersch, R. C. Beardsley, 1974 M.I.T. New England shelf dynamics experiment (March 1974) data report, II, The moored array, Rep. 76-1, Dept. of Meteorol., Mass. Inst. of Technol., Cambridge, 1976.
47. G. Boccaletti, R. Ferrari, B. Fox-Kemper, Mixed layer instabilities and restratification. *J. Phys. Oceanogr.* **37**, 2228 (2007). [doi:10.1175/JPO3101.1](https://doi.org/10.1175/JPO3101.1)
48. P. H. Stone, On non-geostrophic baroclinic stability: Part II. *J. Atmos. Sci.* **27**, 721–726 (1970). [doi:10.1175/1520-0469\(1970\)027<0721:ONGBSP>2.0.CO;2](https://doi.org/10.1175/1520-0469(1970)027<0721:ONGBSP>2.0.CO;2)
49. B. Fox-Kemper, G. Danabasoglu, R. Ferrari, S. M. Griffies, R. W. Hallberg, M. M. Holland, M. E. Maltrud, S. Peacock, B. L. Samuels, Parameterization of mixed layer eddies. III: Implementation and impact in global ocean climate simulations. *Ocean Model.* **39**, 61–78 (2011). [doi:10.1016/j.ocemod.2010.09.002](https://doi.org/10.1016/j.ocemod.2010.09.002)
50. A. Tandon, C. Garrett, Mixed layer restratification due to a horizontal density gradient. *J. Phys. Oceanogr.* **24**, 1419–1424 (1994). [doi:10.1175/1520-0485\(1994\)024<1419:MLRDTA>2.0.CO;2](https://doi.org/10.1175/1520-0485(1994)024<1419:MLRDTA>2.0.CO;2)
51. J. H. Martin, S. E. Fitzwater, R. M. Gordon, C. N. Hunter, S. J. Tanner, Iron, primary production and carbon-nitrogen flux studies during the JGOFS North Atlantic bloom experiment. *Deep Sea Res. Part II Top. Stud. Oceanogr.* **40**, 115–134 (1993).
[doi:10.1016/0967-0645\(93\)90009-C](https://doi.org/10.1016/0967-0645(93)90009-C)